Hydration State of Single Cytochrome c Monolayers on Soft Interfaces via Neutron Interferometry

L. R. Kneller,* A. M. Edwards,† C. E. Nordgren,† J. K. Blasie,† N. F. Berk,‡ S. Krueger,‡ and C. F. Majkrzak‡
Departments of *Physics and †Chemistry, University of Pennsylvania, Philadelphia, Pennsylvania 19104, and ‡Center for Neutron Research, National Institute of Standards and Technology, Gaithersburg, Maryland 20899 USA

ABSTRACT Yeast cytochrome c (YCC) can be covalently tethered to, and thereby vectorially oriented on, the soft surface of a mixed endgroup (e.g., -CH_3/-SH = 6:1, or -OH/-SH = 6:1) organic self-assembled monolayer (SAM) chemisorbed on the surface of a silicon substrate utilizing a disulfide linkage between its unique surface cysteine residue and a thiol endgroup. Neutron reflectivities from such monolayers of YCC on Fe/Si or Fe/Au/Si multilayer substrates with H_2O versus D_2O hydrating the protein monolayer at 88% relative humidity for the nonpolar SAM (-CH_3/-SH = 6:1 mixed endgroups) surface and 81% for the uncharged-polar SAM (-OH/-SH = 6:1mixed endgroups) surface were collected on the NG1 reflectometer at NIST. These data were analyzed using a new interferometric phasing method employing the neutron scattering contrast between the Si and Fe layers in a single reference multilayer structure and a constrained refinement approach utilizing the finite extent of the gradient of the profile structures for the systems. This provided the water distribution profiles for the two tethered protein monolayers consistent with their electron density profile determined previously via x-ray interferometry (Chupa et al., 1994).

INTRODUCTION

Previous optical spectroscopy studies have shown that yeast cytochrome c (YCC) covalently bound to a soft interface and partially hydrated by a moist helium atmosphere at sufficiently high relative humidity can be fully functional with respect to the oxidation-reduction chemistry of its iron porphyrin prosthetic group and reversibly unbound to large extent without loss of function (Pachence et al., 1990; Pachence and Blasie, 1991; Chupa et al., 1994; Edwards et al., 1998). Water of hydration is important for maintaining the structure of soluble proteins, including the membrane protein YCC, so it would be interesting to know how much water hydrates each YCC molecule in such a monolayer as required to maintain protein function. Such partially hydrated membrane protein monolayers are required for structural studies employing both nonresonance and resonance x-ray scattering and x-ray spectroscopic techniques, e.g., at x-ray energies in the neighborhood of the FeK absorption edge.

Unlike x-ray scattering, neutron scattering can be sensitive to different isotopes of the same atom. For instance, the scattering length for neutrons from hydrogen (-0.374×10^{-12} cm), where the minus sign indicates the scattered neutrons are in phase with the incident neutrons upon resonance scattering, is very different from that of deuterium ($+0.667 \times 10^{-12}$ cm), where the plus sign indicates a phase change of π upon potential scattering by convention. Comparing the neutron scattering density profile derived from neutron reflectivity for a YCC monolayer hydrated by D_2O with the same profile for identical hydration with H_2O will yield the water distribution in the monolayer profile structure. An iron-silicon or iron-gold-silicon multilayer structure possessing a silicon surface layer can be used as the solid substrate for the tethered YCC monolayer. Such a multilayer substrate has two key advantages in a neutron (or x-ray) reflectivity measurement. Whereas an organic/bioorganic monolayer on a uniform silicon substrate would scatter only weakly, a multilayer substrate dramatically enhances this scattering for momentum transfer normal to the substrate surface, especially in the range of higher momentum transfer, due to the interference between the scattering from the multilayer substrate and the organic/bioorganic overlayers. A multilayer substrate also provides an important reference profile structure for the unique interferometric phasing of the reflectivity data. The constrained refinement interferometry method, employing the first Born approximation (see Appendix), requires only a single reference structure and was successfully implemented for the phasing of the data in these experiments. In addition, for polarized neutrons, a magnetic reference layer such as iron can yield two different reference structures when the polarized neutrons are incident with their spins either parallel or antiparallel to the magnetization of the reference layer (see Fig. 1). Multiple reference structures for a single specimen allow the possibility of a direct analytic inversion of the reflectivity data (Majkrzak and Berk, 1995). Although the low neutron scattering contrast between the Fe layer and Si (or Au) layer for the antiparallel spin case prevented this phasing method from succeeding in these experiments, the high contrast provided by the parallel spin case was nevertheless important to the success of the constrained refinement phasing method.

Received for publication 7 February 2000 and in final form 19 January 2001.

Address reprint requests to Dr. J. Kent Blasie, Department of Chemistry, University of Pennsylvania, 231 South 34th Street, Philadelphia, PA 19104-6323. Tel.: 215-898-6208; Fax: 215-573-2112; E-mail: jkblasie@sas.upenn.edu.

0006-3495/01/05/2248/14 $2.00

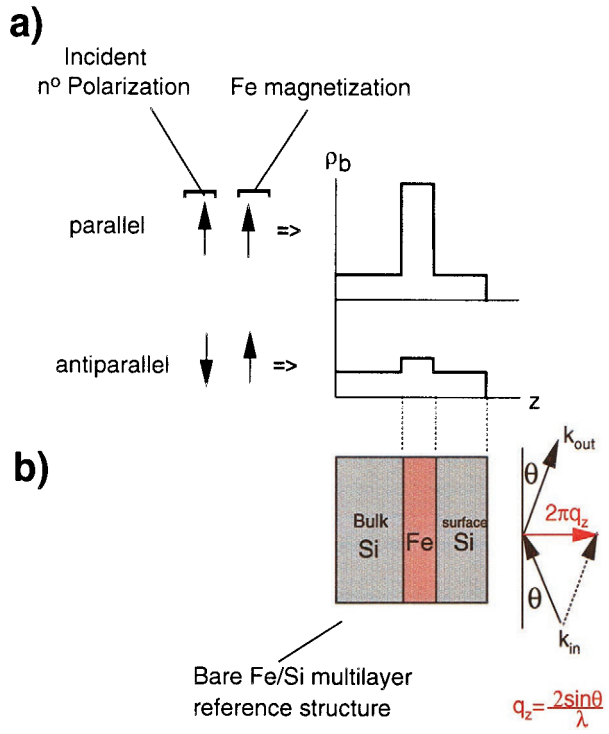

FIGURE 1 Neutron scattering length densities for polarized neutrons depends on the polarization of the incident neutrons relative to the direction of magnetization of the ferromagnetic material. For iron, the scattering length density is either 3.0×10^{-6} Å^{-2} for antiparallel spins or 13.0×10^{-6} Å^{-2} for parallel spins, relative to the spin-independent scattering length density of 2.1×10^{-6} Å^{-2} for Si.

MATERIALS AND METHODS

Nonpolar SAM

Iron-silicon multilayer substrates were fabricated by magnetron sputtering on 4-inch-diameter, 1/2-inch-thick single crystal Si wafers by Osmic (Troy, MI). The nominal layers on bulk Si consisted of a 50-Å Fe layer with a 100-Å-thick Si overlayer (Fig. 2). Neutron reflectivity was then collected for one representative multilayer substrate in this series at the NG1 reflectometer at NIST. NG1 is a two-axis reflectometer with a horizontal scattering plane, a neutron polarizer, and analyzer in the incident and scattered beam, operating on the NIST cold neutron source with an incident neutron wavelength of $\lambda = 4.75$ Å. A different multilayer substrate in this series, which had nearly identical reflectivity over the range of 0.00164 Å$^{-1} \leq q_z \leq 0.0294$ Å^{-1}, was used for the remainder of this experiment, where $q_z = 2\sin\theta/\lambda$ is the momentum transfer normal to the substrate surface divided by 2π.

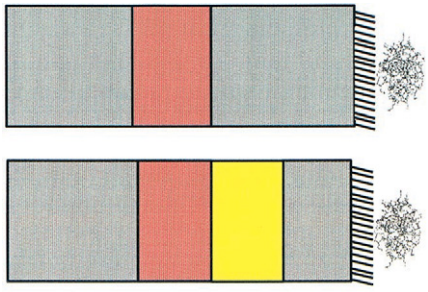

FIGURE 2 Schematic of the nonpolar SAM/cytochrome c system on the Fe/Si multilayer substrate (*top*) and the uncharged-polar SAM/cytochrome c system on the Fe/Au/Si multilayer substrate (*bottom*). The protein is shown as a representation of its x-ray crystal structure. The hydrocarbon chains of the SAM are tilted arbitrarily, and the tilt has not been investigated here.

The multilayer substrate was first cleaned extensively in an evaporation dish with the organic solvents methanol, acetone, and chloroform 10 min each with sonication. The dish was then filled with concentrated nitric acid for 1 min, subsequently rinsed 10 times with Millipore water (18 MΩ cm) and then thoroughly dried. While this concentrated acid treatment is required for the alkylation of silicon and quartz substrates with alkyltrichlorosilanes (due to their processing), it is not required for silicon overlayers deposited on clean silicon substrates by sputtering, electron beam evaporation, or molecular beam epitaxy techniques.

The alkylation solution consisted of 240 ml of hexadecane, 36 ml of carbon tetrachloride, and 24 ml of chloroform. While stirring the solution, 64 drops of dodecyl-trichlorosilane (Hüls America, Bristol, PA) and 11 drops of trichlorylsilyl-undecyl-thioacetate were added to the solution using Becton Dickinson (Mountain View, CA) 3-cc IM 1½ 23 GTW syringes. The multilayer substrate was placed into the alkylation solution in an evaporation dish, and the dish was placed into a sonic bath for 22 min. The solution was then removed, and the substrate was rinsed two times with chloroform and then sonicated in chloroform for 10 min. The multilayer substrate was then dried and stored under argon until needed.

The protected chemisorbed organic self-assembled monolayer (SAM) was deprotected in a mixture containing 50% concentrated HCl and 50% methanol for 45 min (a time much longer than necessary; see below) to yield the -CH_3/-SH = 6:1 mixed endgroup SAM via acid hydrolysis of the thioacetate ester. The SAM's surface was macroscopically nonpolar, established by wetting. After rinsing 10 times in Millipore water, the deprotected alkylated multilayer substrate was placed into a 1 mM Tris buffer (pH 8.0) solution containing yeast cytochrome c (from *Saccharomyces cerevisiae*, Sigma Chemical Co., St. Louis, MO) at 10 mM concentration and incubated for 16 h at 4°C. At the end of that time it was rinsed three times in Tris buffer and then soaked for 45 min in the buffer to remove noncovalently bound protein from the alkylated surface of the wafer. Finally, it was placed in a sealed humid cell over a saturated solution of KNO_3 (96% relative humidity at 4°C) and equilibrated while the reflectometer was aligned.

Uncharged-polar SAM

Because the iron layer was found to be mildly attacked by the acid during the cleaning process in the nonpolar SAM experiment (visual inspection of the substrate's optical reflectivity suggested that the substrate's surface was no longer uniform on a >1-cm length scale), the second experiment used a slightly different multilayer substrate. Iron, gold, and silicon layers were deposited onto a 3-inch by 1-inch by 0.5-mm silicon slide cut from a 4-inch-diameter 0.5-mm-thick silicon wafer by electron-beam evaporation at the Cornell Center for Materials Research (Ithaca, NY). The nominal layers on the bulk Si were a 50-Å Fe layer, a 50-Å Au layer, and a 50-Å-thick Si overlayer (Fig. 2). It was anticipated that the gold layer would better protect the underlying Fe layer from chemical attack. Rocking curves using x-rays were collected on this multilayer substrate before and after deposition of the SAM and protein overlayers utilizing a cylindrically curved LiF(200) focusing monochromator crystal in the incident beam from an Elliott GX-13 rotating-anode x-ray source and a flat LiF(200) analyzer crystal in the nondispersive mode with a scintillation detector to record the scattered beam. Neutron reflectivity data were also collected with the NG1 reflectometer on this multilayer substrate before and after the deposition of the SAM and protein overlayers. The substrate was first cleaned extensively in an evaporation dish with only the organic solvents

methanol, acetone, and chloroform 10 min each with sonication. The cleaning step involving nitric acid was omitted for this substrate because it was found (via x-ray reflectivity) with several others prepared identically that acid cleaning removed the Fe/Au/Si multilayer.

The alkylation solution consisted of 140 ml of hexadecane, 21 ml of carbon tetrachloride, and 14 ml of chloroform. While stirring the solution, 30 drops of trichlorosilyl-acetoxy-undecane and 5 drops of trichlorylsilyl-undecyl-thioacetate were added to the solution using Becton Dickinson 3-cc IM 1½ 23 GTW syringes. The multilayer substrate was placed into the alkylation solution in a glass alkylation vessel that was custom made to reduce needed volumes of chemicals. The vessel containing the substrate and solutions was then placed into a sonic bath for 22 min. The solution was then removed, and the substrate was rinsed two times with chloroform and then sonicated in chloroform for 10 min. The protected chemisorbed organic SAM was deprotected in a mixture containing 50% concentrated HCl and 50% methanol for only 1 min to yield the -OH/-SH = 6:1 mixed endgroup SAM via acid hydrolysis of the thioacetate and acetoxy esters. This was sufficient to render the SAM's surface macroscopically polar, established by wetting. After rinsing 10 times in Millipore water, the deprotected alkylated substrate was placed into a 1 mM Tris buffer (pH 8.0) solution containing YCC (from *S. cerevisiae*, Sigma) at 10 mM concentration and incubated for 16 h at 4°C. At the end of that time it was rinsed three times in Tris buffer and then soaked for 45 min in the buffer to remove noncovalently bound protein from the alkylated surface of the wafer. Finally, it was placed in a sealed humid cell over a saturated solution of KNO_3 (96% relative humidity at 4°C) and equilibrated while the reflectometer was aligned.

Reflectometry

The multilayer substrates with the tethered YCC monolayer on their surface were placed in a sealed temperature-controlled specimen chamber on the ω-axis of the NG1 reflectometer at the Center for Neutron Research, National Institute of Standards and Technology; the specimen chambers were substantially different for the nonpolar SAM and subsequent uncharged-polar SAM cases. Humidity was controlled using a LiCor Li-610 dew point generator (LI-COR, Inc., Lincoln, NE) and moist helium flow through the specimen chamber. Relative humidity and temperature were measured just above the specimen's surface with a Vaisala humidity and temperature transmitter (VAISALA, Inc., Boston, MA), model HMD70Y inside the specimen chamber. Temperature was controlled by a Neslab model RTE-111 chiller (Thermo Neslab, Portsmouth, NH) circulating cooled ethylene glycol through the specimen chamber.

For the nonpolar SAM case, the first half of the experiment was done in helium with D_2O vapor produced by the dew point generator. The relative humidity read by the sensor was 82%. This measurement was somewhat ambiguous, because the humidity probe was calibrated for H_2O vapor. It is known from the swelling of dipalmitoylphosphatidylcholine (DPPC) multilayers that the periodicity of the multilayers as detected by x-ray or neutron diffraction is the same whether the relative humidity used to swell the multilayer is produced by a saturated salt solution containing H_2O or D_2O as the solvent (Zaccai et al., 1975). Saturated salt solutions of KCl (nominally 88% relative humidity) and NaCl (nominally 76%) were used as standards to produce water vapor at constant relative humidity over the range of immediate interest. This relative humidity was then measured using the same humidity probe as for the reflectivity experiments. The measured relative humidities for H_2O and D_2O are shown in Table 1. Based on the relative humidities measured compared with these standards, the humidities during reflectivity measurements were 87.4% for D_2O and 89.3% for the H_2O case.

The transition between the first and second parts of the reflectivity experiment was monitored by observing the reflectivity at a fixed angle ($\theta = 0.8°$, $q_z = 0.00587$ Å^{-1}) after D_2O was replaced by H_2O in the dew point generator. Once this reflectivity had stabilized to a constant value over a 4-h period, reflectivity measurements were begun for the H_2O case (see Fig. 3).

TABLE 1 Table of relative humidities measured by a Vaisala humidity and temperature transmitter, HMD70Y

Salt	Solvent	Measured humidity
KCl	H_2O	86.7%
	D_2O	82.6%
NaCl	H_2O	76.2%
	D_2O	74.2%

For the uncharged-polar SAM case, the relative humidity was maintained at a somewhat lower value of ~81% for D_2O and H_2O, and the changeover was once again monitored by observing the reflectivity at fixed angle, this time at $\theta = 1.75°$.

RESULTS

Each reflectivity data set (H_2O and D_2O) was collected over a 48-h period for the nonpolar SAM case. Data were collected with the iron layer of the substrate magnetically polarized. Incident neutrons were polarized with their spins either parallel or antiparallel to the iron magnetization. Thus, data for two relative polarizations were collected at each value of momentum transfer for each type of water. However, only the parallel spin case, where there is maximal neutron scattering contrast in the reference multilayer, could be analyzed by the constrained refinement method (see Discussion below).

Each reflectivity data set (H_2O and D_2O) was collected for the uncharged-polar SAM case over only a 24-h period due to time constraints arising during the experimental run. Data were again collected with the iron layer of the substrate magnetically polarized. Incident neutrons were polarized with their spins either parallel or antiparallel to the iron magnetization. Thus, data for two relative polarizations were collected at each value of momentum transfer for each type of water. In this case, data for the antiparallel case were analyzed using the constrained refinement method (described below) and, allowing for the much larger errors involved due to the necessarily poorer counting statistics, yielded results that were consistent with the parallel case (as shown below).

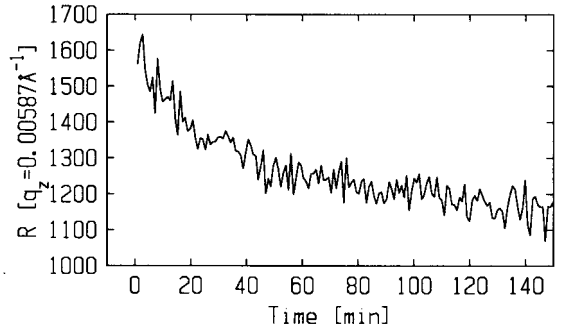

FIGURE 3 Neutron reflectivity at $\theta = 0.8°$ ($q_z = 0.00587$ Å^{-1}) monitored during changeover from D_2O to H_2O for the nonpolar SAM case.

All neutron reflectivity data were first divided by the Fresnel function to yield the normalized reflectivity data, namely, the modulus squared of the Fourier transform of the gradient of the scattering length density profile for the specimen (see Appendix for details). Profile refers here to the projection of the scattering length density of the specimen parallel to the plane of the surface onto the normal to the surface, e.g., the z axis. This rigorously removes the reflectivity from a uniform substrate with an infinitely sharp interface at its surface from the data.

It is clear from the resulting normalized reflectivity data that significant changes occurred upon addition of the organic SAM and protein overlayers (see Fig. 4). Significant changes in the scattering are also seen following changeover from D_2O to H_2O. For the specimen with a nonpolar SAM, the reflectivity was studied for elastic momentum transfer out to $q_z = 0.0637$ Å^{-1}, with a good signal-to-noise ratio. For the specimen with an uncharged-polar SAM, the reflectivity was studied for elastic momentum transfer only out to $q_z = 0.0477$ Å^{-1}, with a good signal-to-noise ratio, due to the necessarily shorter data collection time permitted.

The gradient of the scattering length density profile for both the Fe/Si and Fe/Au/Si multilayer substrates contain relatively large-amplitude features due to the sharpness of the interfaces and the scattering density contrast across the interfaces therein, and their profile structures are essentially known from their fabrication specifications. Conversely, the SAM/protein overlayers make a relatively small contribution to the gradient of the profile structure of the composite system because the gradients of their scattering length density profiles are expected to contain much broader, smaller-amplitude features compared with those of the multilayer substrates. This known multilayer substrate profile structure can then be used as the reference structure to determine the profile structures of the unknown SAM/protein overlayers by neutron interferometry in the kinematical limit (see Appendix for details), first described for x-rays by Lesslauer and Blasie (1971), as indicated below. The normalized neutron reflectivity for the composite structures can be expressed in the kinematical limit for $q_z > q_{critical}$ by the equation

$$|\Phi_{kin}(q_z)|^2 = |\Phi_k(q_z)|^2 + |\Phi_u(q_z)|^2 + 2|\Phi_k(q_z)||\Phi_u(q_z)|\cos\{[\psi_k(q_z) - \psi_u(q_z)] + 2\pi q_z A_{ku}\}, \quad (1)$$

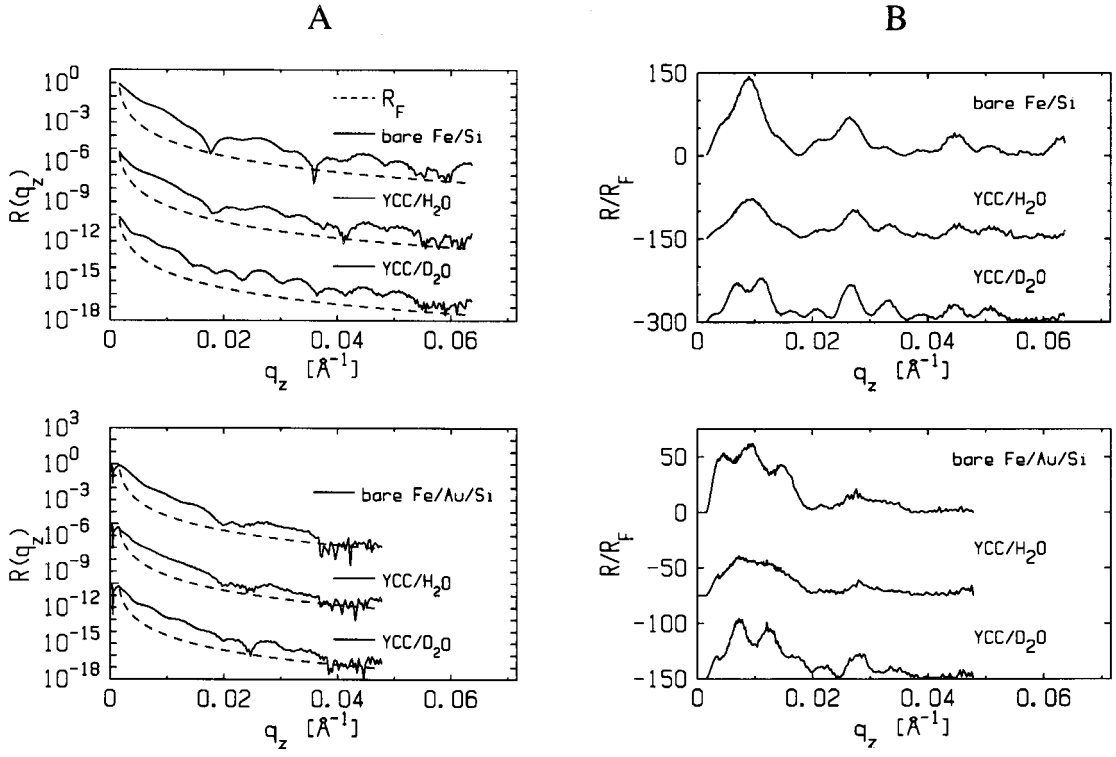

FIGURE 4 (*A*) Raw reflectivities for the bare multilayer substrate, substrate plus nonpolar SAM plus YCC/D_2O, and substrate plus nonpolar SAM plus YCC/H_2O (*top*) and similarly for the substrate plus uncharged-polar SAM plus YCC (*bottom*) for the incident neutron spins parallel to the iron magnetization. The H_2O data are offset by 10^{-5} and the D_2O data by 10^{-10} units on the ordinate. (*B*) Normalized reflectivity data for the bare multilayer substrate, substrate plus nonpolar SAM plus YCC/D_2O, and substrate plus nonpolar SAM plus YCC/H_2O (*top*) and similarly for the substrate plus uncharged-polar SAM plus YCC (*bottom*) for the incident neutron spins parallel to the iron magnetization. In the top plot the H_2O data are offset by 150 units and the D_2O data by 300 units on the ordinate and in the bottom plot the H_2O data are offset by 75 units and the D_2O data by 150 units on the ordinate.

where $|\Phi_{kin}(q_z)|^2$ is the modulus squared of the Fourier transform of the gradient of the neutron scattering length density profile for the composite structure and $|\Phi_k|^2$ and $|\Phi_u|^2$ are the moduli squared of the Fourier transforms of the gradients of the neutron scattering length density profiles for the known multilayer substrate and the unknown SAM/protein overlayers, respectively. The modulus squared of these three Fourier transforms can, in principle, be determined experimentally from the neutron reflectivities from the multilayer substrate itself, from the SAM/protein overlayer on a uniform Si substrate, and from the composite structure. ψ_k and ψ_u are the phases of their respective Fourier transforms, where ψ_k is known (because the profile, and hence the gradient, of the reference multilayer substrate is known, and therefore its Fourier transform is known uniquely) and ψ_u is unknown. Each is referenced to the center of mass of its respective profile, and A_{ku} is the distance along the z axis between the centers of mass of the multilayer substrate and the SAM/protein overlayer. If, instead, we reference the center of mass of the profile of the unknown overlayer structure to the center of mass of the profile of the known multilayer reference structure via the substitution $\psi'_u = \psi_u - A_{ku}$, application of Eq. 1 above can provide the unknown ψ'_u as a function of q_z. A unique inverse Fourier transform utilizing the experimental modulus, $|\Phi_u(q_z)|$, and the thereby determined $\psi'_u(q_z)$ then provides the gradient of the unknown profile structure of the SAM/protein overlayer, and ultimately the profile itself by integration. The effect of the last term of Eq. 1 above, which corresponds to the critical interference between the strong kinematical reflectivity from the multilayer substrate and the weak kinematical reflectivity from the overlayer required to recover the otherwise unknown phase information, ψ'_u, is readily apparent from the differences between the normalized kinematical reflectivity from the bare multilayer substrate and that for the composite multilayer substrate-SAM/protein overlayer specimen hydrated with either H_2O or D_2O, as shown in Fig. 4.

For $q_z > 0.00164$ Å^{-1}, namely, $q_{critical}$ for neutrons incident on silicon, the $|\Phi_{kin}|^2$ for both the bare multilayer substrate and the composite multilayer substrate/organic/bio-organic overlayer specimen were assumed to be obtained from the normalized reflectivity data as described (see Appendix).

Neutron interferometric analysis of the normalized reflectivity data in the kinematical limit was performed using a highly constrained real-space refinement algorithm in a manner entirely analogous to that fully described previously for the x-ray case (Xu et al., 1991) to accomplish the interferometric phasing of these data, with the exception that we here employ the gradient of the scattering density profile whereas prior work with x-rays employed the scattering density contrast profile (see Appendix for further details). The constrained refinement approach has proven to be significantly more robust than the procedure described above, which requires a point-by-point comparison of moduli of three Fourier transforms as a function of q_z to recover the unknown phase information. This method of analysis involved first establishing the gradient of the neutron scattering profile for the bare Fe/Si or Fe/Au/Si substrate, with the initial models for the substrate being constructed on an absolute scattering length density scale based on their respective fabrication specifications. The gradients of these model profiles were calculated and the model parameters were then relaxed via a model refinement analysis by comparing the calculated modulus squared of the Fourier transform of the gradient profile and its unique inverse Fourier transform, the Patterson function (i.e., the autocorrelation of the gradient profile in this case), for the models with their corresponding experimental counterparts, the Patterson functions for the models being subject to the same q_z window as the experimental normalized reflectivity data ($(q_z)_{min} = 0.00164$ Å$^{-1} \leq q_z \leq (q_z)_{max} = 0.0637$ Å^{-1} for the nonpolar case and $(q_z)_{min} = 0.00164$ Å$^{-1} \leq q_z \leq (q_z)_{max} = 0.0477$ Å^{-1} for the polar SAM case). Once reasonable (i.e., close but not perfect) agreement had been achieved between the experimental functions and their model counterparts, the constrained real-space refinement algorithm was employed as a final relaxation procedure (see following paragraph). The interior portion of the resulting model neutron scattering length density gradient profile for the bare Fe/Si multilayer substrate, $[d\rho_{mod}(z)/dz]_{substrate}$ was utilized as a primary constraint. This procedure yielded the experimental neutron scattering density gradient profile for the bare substrate, $[d\rho_{exp}(z)/dz]_{substrate}$, which predicted exactly both the experimental normalized reflectivity from the substrate and its unique inverse Fourier transform, the Patterson function. Only the interior portion of this known scattering length density gradient profile was then used as the reference structure for the constrained real-space refinement of the normalized neutron reflectivity for the multilayer substrate/SAM/cytochrome c system because of the modification of the silicon surface of the substrate that occurs upon formation of the SAM on its surface by chemisorption (Xu et al., 1993).

The constrained real-space refinement algorithm provides one solution among a finite number of possible solutions for the phase of the Fourier transform of the gradient of the neutron scattering density profile. The algorithm utilizes the phase dominance of the gradient profile of the known reference multilayer structure to force the box-refinement algorithm, which uses the finite extent of the gradient profile for the specimen obtained directly from the Patterson function as an additional constraint, to converge to the local gradient profile structure most similar to the gradient of the reference profile structure (Stroud and Agard, 1979; Makowski, 1981). The resulting determined experimental gradients of the neutron scattering density profiles for the nonpolar and uncharged-polar SAM cases, each partially hydrated with either H_2O or D_2O, are shown as $[d\rho/dz]_{exp}$ in

Fig. 5. Their integration to provide the absolute neutron scattering density profile $\rho_{exp}(z)$ for each case was achieved via a real-space model refinement of a parameterized model for $\rho_{mod}(z)$ until $[d\rho/dz]_{mod}$ reached perfect agreement with the corresponding $[d\rho/dz]_{exp}$, also shown in Fig. 5 for each case.

DISCUSSION

Both the constrained refinement interferometric method, in the kinematical limit, and the direct analytic inversion interferometric method, in the dynamical limit, could utilize both the parallel and antiparallel spin polarization cases to provide the same neutron scattering density profiles for the bare multilayer substrates before their alkylation (not shown here) This is consistent with the comparison of the kinematical and dynamical scattering approaches presented in the Appendix of Lösche et al., 1993. The normalized reflectivity data for the parallel spin polarization case provided physically reasonable results, summarized in Fig. 6 *A*, when analyzed using the constrained refinement interferometric phasing method, which requires only a single set of

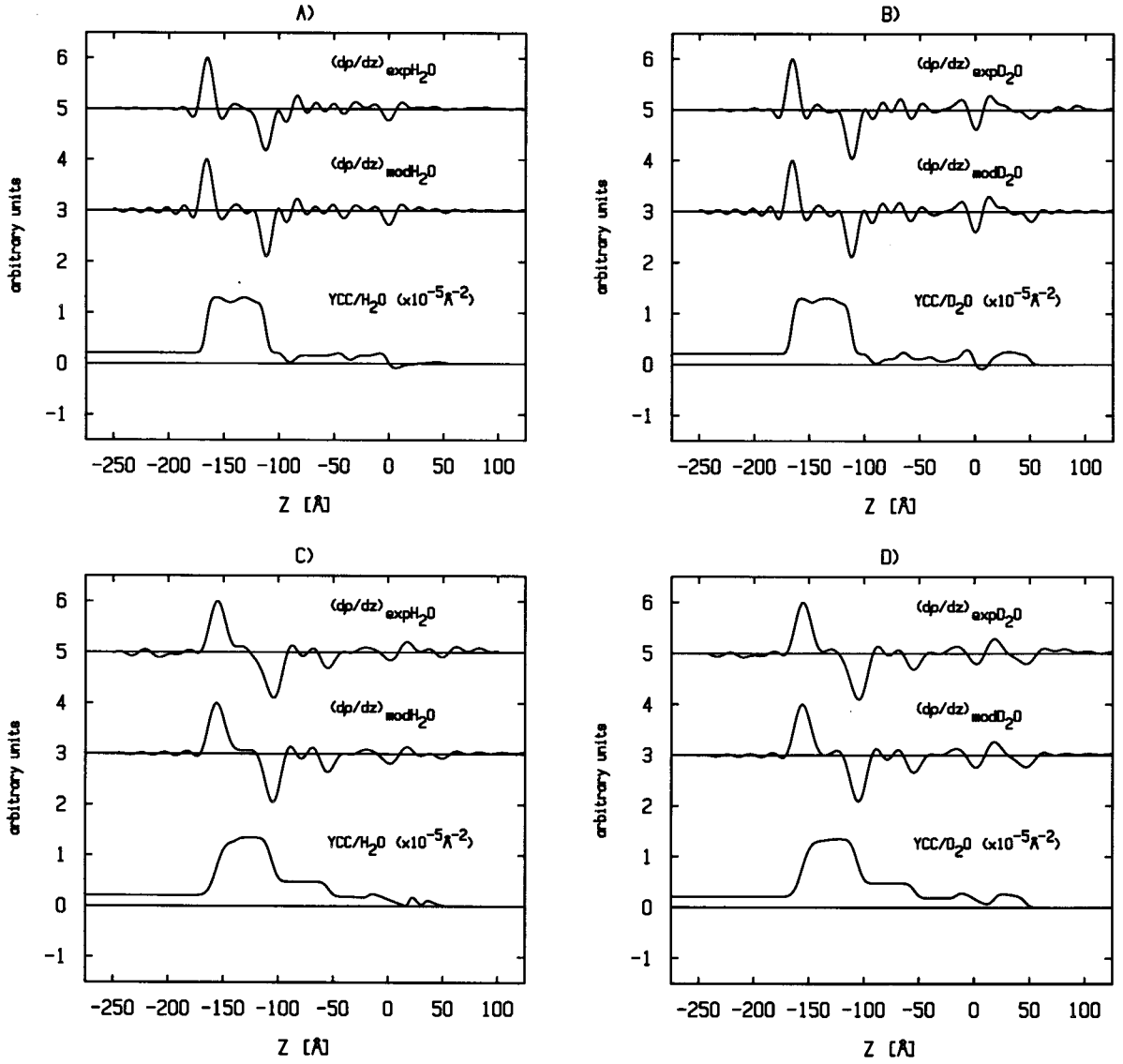

FIGURE 5 The gradients of the neutron scattering density profiles $[d\rho/dz]_{exp}$ for both the nonpolar SAM for partial hydration with H_2O (*A*) and D_2O (*B*) and uncharged-polar SAM cases for partial hydration with H_2O (*C*) and D_2O (*D*), as determined by the constrained refinement implementation of the interferometric phasing of their respective normalized neutron reflectivity data. The incident neutron spins were parallel to the magnetization of the Fe layer in all cases shown. The integration of $[d\rho/dz]_{exp}$ to provide, respectively, the absolute neutron scattering density profile $\rho_{exp}(z)$ for each case was achieved via a real-space model refinement of a parameterized model for $\rho_{mod}(z)$ until $[d\rho/dz]_{mod}$ reached perfect agreement with the corresponding $[d\rho/dz]_{exp}$ is also shown here.

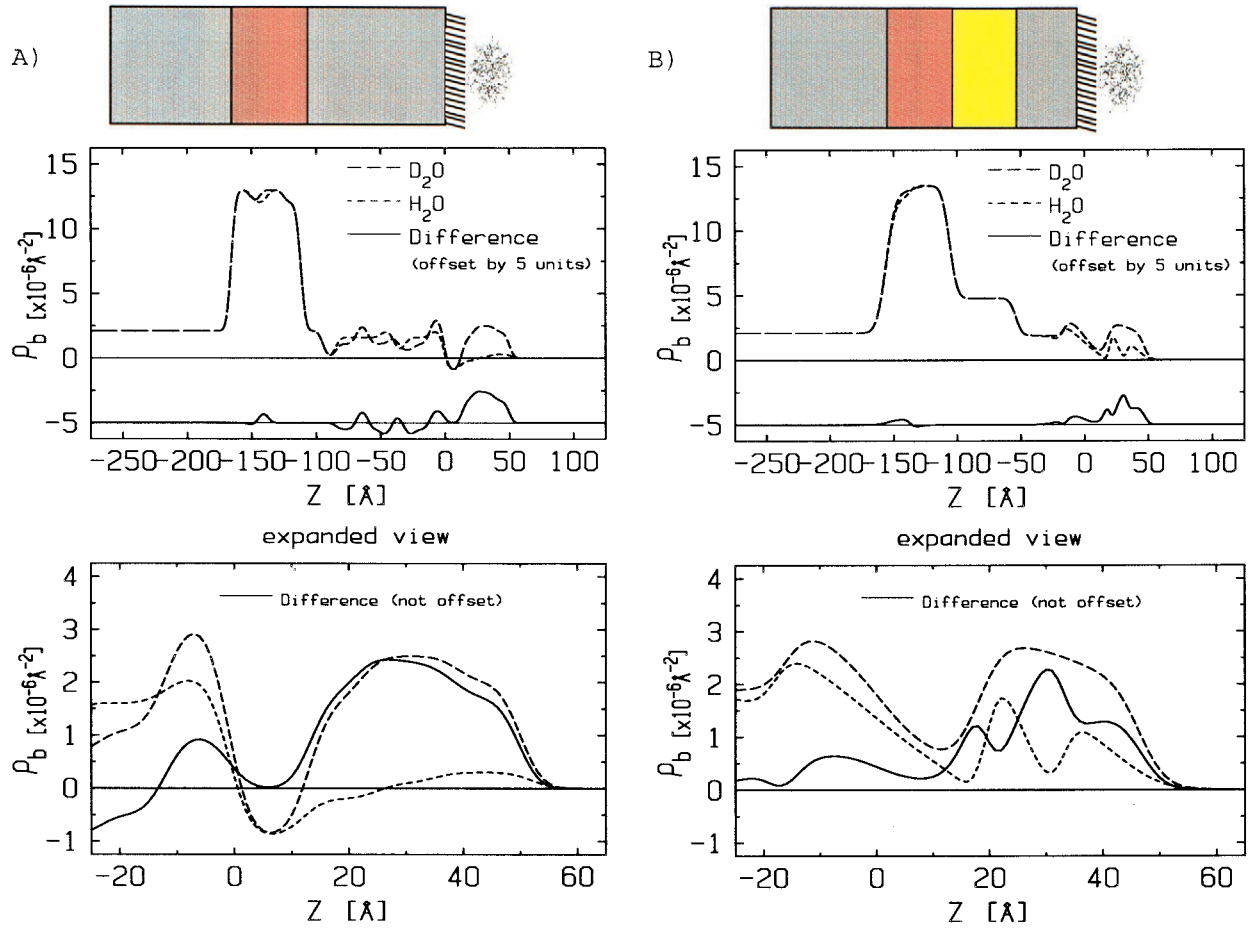

FIGURE 6 The absolute neutron scattering length density profiles with incident neutron spins parallel to the iron magnetization for partial hydration with D_2O and H_2O and their difference profile for both the nonpolar SAM (*A*) and uncharged-polar SAM (*B*) cases. The boundaries for the cytochrome c protein region of the profiles used for calculation of the amount of water hydrating the protein are $z = 10$ Å and $z = 60$ Å. A schematic of the composite structures for both the nonpolar SAM and uncharged-polar SAM cases are shown above the absolute neutron scattering length density profiles approximately to scale.

normalized neutron reflectivity data. Indeed, the results for the nonpolar SAM/YCC profile structure obtained here are in good agreement with the results previously obtained via x-ray interferometry, allowing for the different spatial resolutions in the profiles as shown in Fig. 7. However, the results for the antiparallel spin polarization case for the nonpolar SAM were rejected due to their unphysical nature by both methods of interferometric analysis. [Upon the changeover from D_2O to H_2O, the constrained refinement interferometric analysis of the reflectivity data indicated the presence of substantial changes throughout the scattering length density profile of the composite structure, including the inorganic multilayer substrate where such changes should be minimal. The inversion method, which relies on the quality of both the antiparallel and parallel spin polarization data sets, provided a substantial imaginary component to the specimen's neutron scattering length density profile, which must necessarily be real.] We speculate that the reason the analysis of the parallel spin polarization data succeeded whereas the analysis for the antiparallel spin polarization did not, is that diffuse scattering arising from acid-induced interfacial roughening can compete more effectively with the specular reflectivity from the Fe/Si interfaces for the antiparallel case. [This competition would reduce the specular reflectivity, especially at lower values of q_z as was observed when the Fe layer has approximately the same scattering length density as Si, i.e., when the neutron scattering density contrast within the reference multilayer profile structure is minimal. We had no capability at the time to investigate this possibility directly via the collection of rocking curves for selected values of q_z, either using neutrons (very inefficient) or x-rays (much more time efficient) under otherwise identical conditions for the very-large-diameter specimen required for the neutron reflectivity. However, in the parallel spin case, where the iron layer has much greater scattering length density than silicon, specular reflectivity from the Si/Fe interfaces and its interference with the specular reflectivity from the organic/bio-organic overlayer can dominate over the diffuse scattering arising from interfacial roughness.] Once the absolute neu-

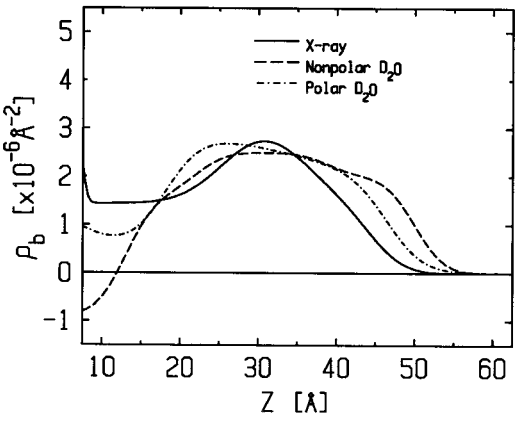

FIGURE 7 The neutron scattering length density profile for the D_2O case for both the nonpolar SAM and the uncharged-polar SAM as compared with the corresponding electron density profile determined previously by x-ray interferometry. The electron density profile shown was for the case of an all-thiol endgroup SAM, which would be comparable in polarity to the uncharged-polar SAM employed in these neutron interferometry studies. Given the very different physical origin of x-ray and neutron scattering, the amplitude of the electron density profile has been arbitrarily scaled here to best match those of the neutron scattering length density profiles. The spatial resolution, here taken as the minimum wavelength Fourier component, for the two neutron scattering length density profiles (namely, ~16 Å and ~21 Å, respectively, for the nonpolar and uncharged-polar SAMs) was substantially less than that for the electron density profile (namely, ~10 Å). More importantly, in terms of the different spatial resolutions, the centers of mass of the cytochrome c molecules occur at the same distance from the substrate surface, namely, ~30 Å, for the electron density profile and the neutron scattering length density profile for the uncharged-polar SAM profile, and at only a slightly larger value of 33–34 Å for the nonpolar SAM case. These key distances are readily resolved in all three profiles.

tron scattering density profile structures for partial hydration with D_2O and H_2O were determined via the constrained refinement approach for the parallel spin case, the difference between them was calculated to yield the water distribution profile for the nonpolar SAM/tethered cytochrome c monolayer, as shown in Fig. 6 *A*.

In previous x-ray interferometry experiments utilizing Ge reference layers, the reference multilayer structure was resistive to acid attack and the specular scattering was dominant over the diffuse scattering over the range of q_z investigated, as demonstrated by rocking curve analysis. For the subsequent work with the uncharged-polar SAM, the substrates were fabricated with a silicon capping layer and a layer of gold covering the iron reference layer. Additionally, more mild cleaning and SAM deprotection procedures were used. It was anticipated that the substrates would have all of the features of the Fe/Si substrate but that they would resist chemical attack (see Materials and Methods). The normalized reflectivity data for the parallel spin polarization case provided physically reasonable results, summarized in Fig. 6 *B*, when analyzed using the constrained refinement interferometric phasing method, which uses only a single set of normalized neutron reflectivity data. Again, the results for the uncharged-polar SAM/YCC profile obtained here are in good agreement with the results previously obtained via x-ray interferometry (see Fig. 7). For the uncharged-polar SAM case, the antiparallel polarization also yielded profile structures that were consistent with the parallel spin case when larger errors due to relatively poorer counting statistics are taken into account. Furthermore, x-ray rocking curves collected on the specimen at selected values of q_z before and after the addition of the bio-organic overlayers showed that diffuse scattering was minimal and dominated by the specular reflectivity over the entire range of q_z investigated. Nevertheless, the direct analytic inversion the spin-polarization-dependent normalized neutron reflectivity data has not been attempted for the uncharged-polar SAM case due to the necessarily relatively poorer counting statistics for the antiparallel spins case, i.e., when the neutron scattering density contrast within the reference multilayer profile structure is minimal. Once the absolute neutron scattering density profile structures for partial hydration with D_2O and H_2O were determined via the constrained refinement approach for the parallel spin case, the difference between them was calculated to yield the water distribution profile for the uncharged-polar SAM/tethered cytochrome c monolayer, as shown in Fig. 6 *B*.

Given these water distribution profiles so obtained (Fig. 6, *A* and *B*), the number of water molecules hydrating the YCC monolayer for each SAM could be calculated. To do this, one must allow for the well-known proton exchange in the cytochrome c molecule itself. Using information on equine cytochrome c as a close approximation, ~17 polypeptide backbone hydrogens were expected to exchange on the time scale of the experiment (Milne et al., 1997). In addition, 104 side-chain hydrogens were expected to exchange quickly relative to the time scale of the experiment (Milne et al., 1997). Allowing for this exchange and integrating the absolute scattering length density profiles for partial hydration with D_2O versus H_2O over the protein region (by summation over the protein for Δz = 1-Å intervals) for the D_2O and H_2O profiles, one can obtain the following two equations for partial hydration with D_2O and H_2O, respectively:

$$\sum_{z=10A}^{60A} \rho_b(z)\Delta z = (N/A)[b_{YCC} + (b_D - b_H)N_{exch} + b_{D2O}N_{water}]$$

and

$$\sum_{z=10A}^{60A} \rho_b(z)\Delta z = (N/A)[b_{YCC} + b_{H2O}N_{water}],$$

where b is the scattering length of the referenced molecule, and N/A (the area density of the protein monolayer) and

N_{water} (the number of water molecules within the protein region of the profile) are the two unknowns to be solved for. Solving these two simultaneous equations places more stringent requirements on the errors in the derived water distribution profiles. The magnitude of these errors is readily apparent from the magnitude of the features within the multilayer substrate region of the profiles where there should be no water; these errors can be seen from Fig. 6 to be on the order of 20–25% for the nonpolar and uncharged-polar SAM cases. However, the area per cytochrome c molecule for both SAM surfaces has been consistently found to be ~1000 Å^2/molecule using optical absorption spectroscopy and optical linear dichroism (Edwards et al., 1998). If, instead, we therefore assume this value for the area per molecule obtained independently from the optical absorption spectroscopy, we can then utilize the following expression for the difference neutron scattering density profile for partial hydration with D_2O versus H_2O containing the one unknown N_{water}:

$$\sum_{z=10A}^{60A} \Delta\rho_b(z)\Delta z = (N/A)[N_{exch}(b_D - b_H) + N_{water}(b_{D2O} - b_{H2O})].$$

We thereby obtain values for $N_{water} \cong 167$ for the uncharged-polar SAM case and $N_{water} \cong 297$ for the nonpolar SAM case. If we assume that the errors in the water distribution profiles arise for the case of partial hydration of the monolayers with H_2O, which is reasonable given that the protein monolayer appears to be nearly contrast matched especially for the nonpolar SAM case, then the first approach using two equations and two unknowns provides similar values for N_{water}, respectively, for the two SAMs and values for N/A consistent with the optical absorption spectroscopy for both SAMs.

Not knowing beforehand how much water was associated with the protein monolayer at the particular relative humidities chosen, perhaps it was not unreasonable to compare partial hydration with D_2O versus H_2O. Furthermore, the relative humidities employed (81% and 88%) are at the low end of those normally utilized to maintain the fully functional state of the cytochrome c, namely, >90%. This was mostly a result of the humidity generator coupled with the specimen chambers, which were different for the two experiments. A more reliable method of determining the water distribution profile and content for these tethered protein monolayers would have been to systematically vary the relative concentrations of H_2O and D_2O in the vapor phase, collect neutron reflectivity over a range of these values, and perform a least-squares analysis of the data, as has been the traditional case for neutron diffraction from thick oriented multilayers. Such an analysis would have provided the neutron scattering contrast match for the protein much more precisely, and the percentage errors for the mixed cases would have been much smaller. However, time constraints prevented such an exhaustive experimental treatment of the uncharged-polar SAM and nonpolar SAM cytochrome c systems at this time.

Because the amount of water needed to maintain oxidation/reduction function of cytochrome c in the tethered monolayers can be provided using the conditions of this experiment, it is interesting to note that 167 water molecules for the uncharged-polar SAM case cover only ~15% of the solvent-accessible surface of the protein as calculated by the program MOLMOL, and 297 water molecules for the nonpolar SAM case cover only ~27%.

To complement these first measurements of the hydration state of the cytochrome c molecules in these tethered monolayers, molecular dynamics computer simulations are being performed. For the nonpolar SAM, the model system is a YCC molecule (initial configuration taken from the x-ray crystal structure) covalently bonded via a disulfide linkage from its surface cysteine residue to an isolated thiol endgroup at an otherwise methyl endgroup surface of an organic SAM; water molecules were also included, at either 500 or 100 water molecules per cytochrome c molecule, to mimic a humid inert atmosphere, noting that the experimentally determined $N_{water} \cong 167$ for the uncharged-polar SAM case and $N_{water} \cong 297$ for the nonpolar SAM case are within this range. For the uncharged-polar SAM, the methyl endgroups were replaced by thiol endgroups, the dipole moments of hydroxyl and sulfhydryl endgroups being similar. Appropriate periodic boundary conditions were used to model an extended monolayer system. The simulations were done using CHARMM, at 300 K, with an all-atom model for the SAM and a polar hydrogen model for the protein. After 600 ps of equilibration, 300 ps of statistics were collected for each system. From these data, the average water distribution profiles were determined for both SAM systems. At this point in our simulations, there is only qualitative agreement between the experimentally derived water distribution profiles and the simulations, allowing for the finite spatial resolution of the experimental profiles, as shown in Fig. 8. Namely, for the nonpolar SAM case, the water distribution profiles are relatively uniform over the extent of the protein profile, and conversely, for the uncharged-polar SAM case, the water distribution profiles are nonuniform exhibiting some more pronounced features over the extent of the protein profile. However, from the protein profiles shown in Fig. 7 for hydration with D_2O, it can be seen that the protein monolayer is 3–4 Å closer to the substrate surface for the uncharged-polar SAM case as compared with the nonpolar SAM case. This result is in excellent agreement with the simulations, as shown in Fig. 9, which show that this arises because side chains of the cytochrome c penetrate the endgroups of the uncharged-polar SAM whereas they do not for the nonpolar SAM case. In the near future, these simulations will be extended to include the much-shorter-range in-plane positional ordering

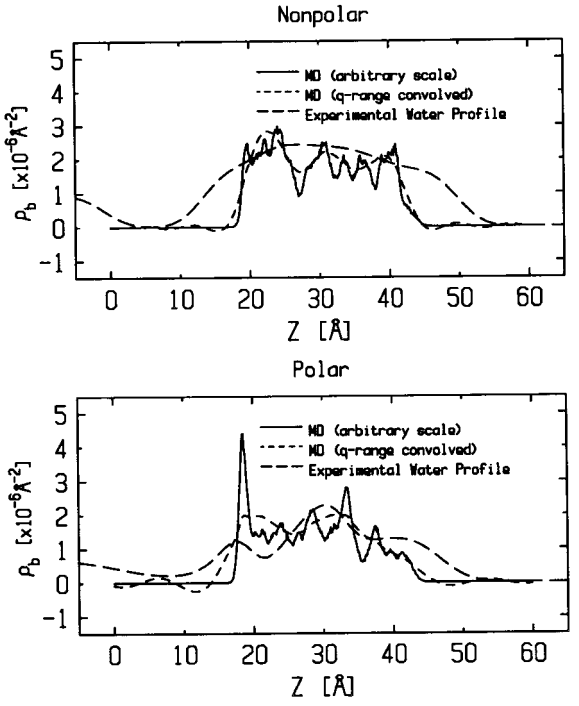

FIGURE 8 Time-averaged water distribution profiles (solid, scaled arbitrarily) from the Molecular Dynamics computer simulations for yeast cytochrome c covalently tethered to the soft surface the nonpolar SAM (*top*) and the uncharged-polar SAM (*bottom*). These simulated atomic-resolution profiles were convoluted with the spatial resolution function appropriate for the experimentally determined water distribution profiles yielding the corresponding resolution-limited profiles (*short dashed line*) from the simulations. The experimentally determined water distribution profiles are shown in long dashes (units of 10^{-6} Å^{-2}). At this point in the simulations, there is only qualitative agreement between the simulations and experiment (see text) most likely arising from insufficient disorder in the model employed for the SAMs.

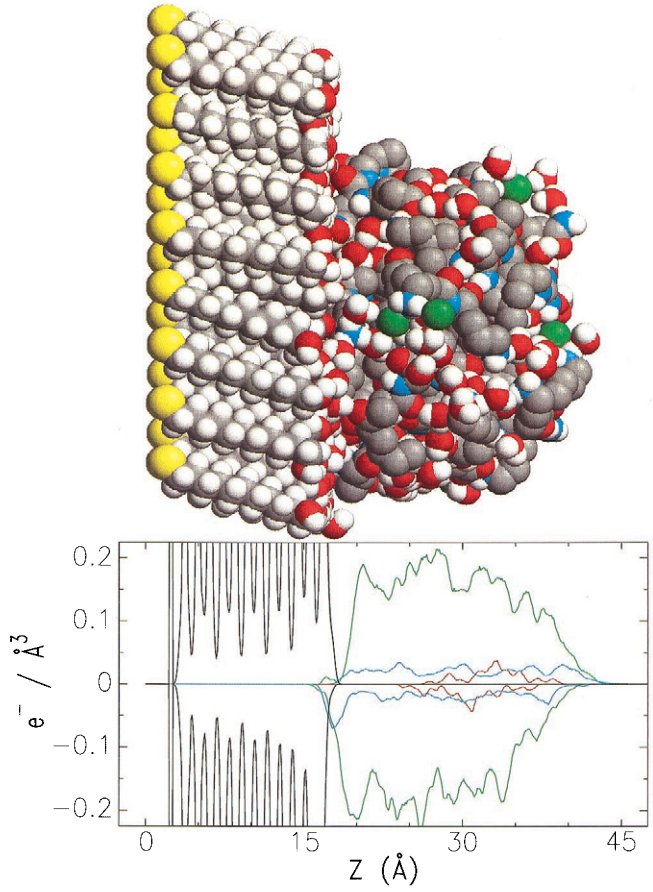

FIGURE 9 An instantaneous configuration at 1400 ps from the Molecular Dynamics computer simulations for yeast cytochrome c covalently tethered to the soft surface of the uncharged-polar SAM (*top*) for a water/cytochrome c mole ratio of 100:1, following equilibration of the ensemble over 1300 ps (yellow-sulfur, gray-carbon, white-hydrogen, red-oxygen, blue-nitrogen, green-chloride). The upper half of the lower portion contains the calculated electron density profiles for the SAM (black), the cytochrome c (green), the cytochrome heme group (red), and the hydrating water (blue) averaged over 200 ps of the trajectory following the 1300-ps equilibration of the ensemble. The lower half of the lower portion contains the corresponding profiles calculated from the Molecular Dynamics simulations for the uncharged-polar SAM case, but inverted to utilize the same abscissa and thereby facilitate the comparison of the two SAM cases. The different positions of the cytochrome c profile relative to the substrate surface for the two SAM cases is readily apparent and in excellent agreement with the experimental neutron scattering length density profiles shown in Fig. 7.

of the SAM hydrocarbon chains known to occur for such alkytrichlorosilane-based SAMs (Xu et al., 1993); this is coupled to disordering of the chain endgroups in the monolayer profile structure arising from gauche/antigauche defects in the intramolecular chain configurations, which in turn would broaden the profile features of the protein and its hydrating water. By modeling these two different SAM/tethered protein systems and predicting a number of critical experimentally accessible structural parameters, including such water distribution profiles, we can gain further insight into the mechanism by which the protein-membrane interaction affects the structure-function relationship for this electron transport membrane protein.

CONCLUSIONS

Neutron interferometry was used to investigate for the first time the water distribution profile within a single monolayer of YCC covalently tethered to both uncharged-polar and nonpolar soft interfaces. The normalized neutron reflectivity was analyzed successfully using an iterative constrained refinement method. For the nonpolar SAM system, the data collected with the incident neutron spins parallel to the iron layer's magnetization within the multilayer substrate provided physically reasonable results, whereas the uncharged-polar SAM system provided physically reasonable results for both parallel and antiparallel neutron spin polarizations. These results, which are fully consistent with independent prior results obtained via x-ray interferometry, showed that a YCC monolayer has ~167 water molecules hydrating

each protein molecule when bound to an uncharged-polar soft interface and ~297 water molecules hydrating each protein molecule when covalently bound to a nonpolar soft interface when partially hydrated with moist helium at 81% and 88% relative humidities, respectively. For this minimal degree of hydration, water covers ~15% of the solvent-accessible surface of the protein in the uncharged-polar SAM case and ~27% in the nonpolar SAM case, and the theoretical water profiles produced from molecular dynamics simulations of the two systems agree at least qualitatively with the experimentally determined water profiles. Future work with this system will include investigation of the water of hydration as a function of relative humidity at higher spatial resolution experimentally in conjunction with ever more realistic molecular dynamics simulations. It is important to note that such results can now be reliably obtained employing a single multilayer reference structure because adequate neutron beam time is limiting.

APPENDIX

Box refinement utilizes the finite extent of a profile structure as a powerful constraint to provide an iterative, model-independent method for obtaining the phase of (and thereby recovering the electron density or neutron scattering length density profile that gave rise to) the scattered intensity collected in an x-ray or neutron reflectivity experiment (Stroud et al., 1979; Makowski, 1981). A unique solution for the profile structure can be obtained only if it can be shown that several very different trial structures refine to the same structure because, for asymmetric profile structures, solution space contains multiple correct profile structures and box refinement will converge to a solution that is the closest structure to the trial structure in the solution space (Makowski, 1981).

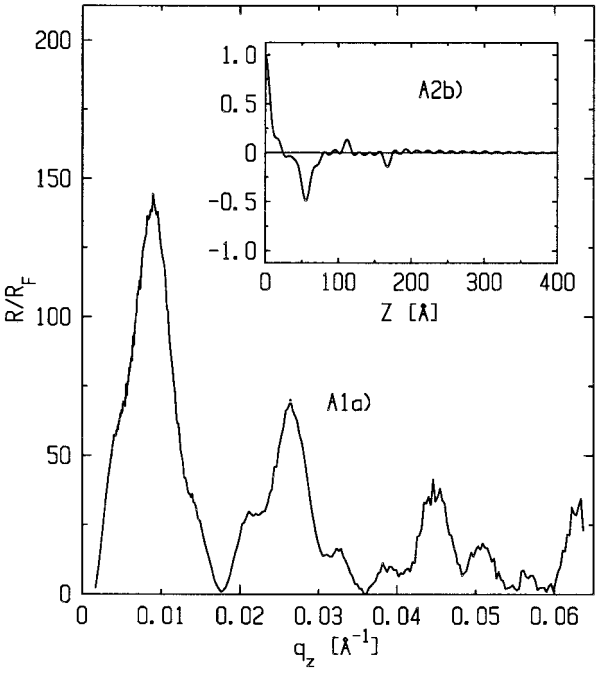

FIGURE 10 Normalized reflectivity for the bare Fe/Si substrate used for measurements of cytochrome c on the nonpolar SAM (*A1a*) and the Patterson function calculated from the reflectivity (*inset*, *A2b*).

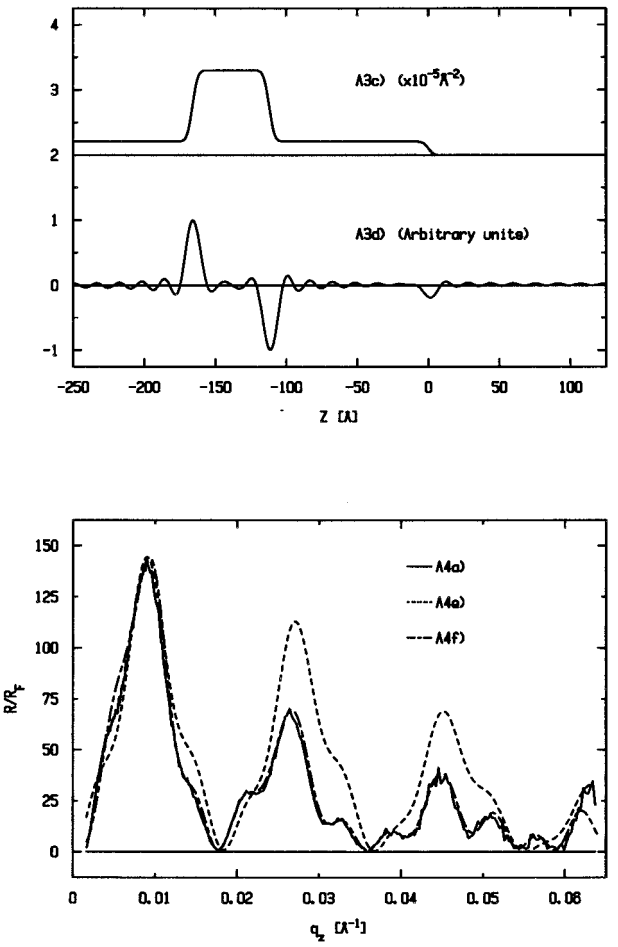

FIGURE 11 (*A3c*) Model produced in the model refinement procedure. This model was differentiated and then Fourier transformed/inverse Fourier transformed to produce the trial function (*A3d*) for highly constrained box refinement. (*A4*) Comparison of the normalized reflectivities calculated from the trial structure (*A4e*) and the constrained refinement output (*A4f*) with the experimental normalized reflectivity (*A4a*).

The highly constrained box-refinement approach to interferometric phasing therefore applies an additional constraint on the data to provide a unique profile structure that correctly predicts the experimentally observed reflectivity. Our group has used this method successfully to solve for the electron density profile structures for a variety of fatty acid and protein ultrathin films on solid substrates (Murphy et al., 1993; Chupa et al., 1994; Prokop et al., 1996; Edwards et al., 1998). In this paper we use it to solve for the neutron scattering length density profile of a tethered protein ultrathin film.

The highly constrained box-refinement approach to interferometric phasing uses three criteria to refine reflectivity data.

First, the structure must be of finite extent. This is true here for the gradient of the profile structure of tethered cytochrome c monolayer films, namely, in the direction perpendicular to the monolayer/solid substrate interface, as it has been for electron density contrast profile of the monolayer/multilayer ultrathin films on solid substrates to which we have already applied the algorithm in x-ray interferometry studies.

Second, the data being analyzed must be in the kinematical limit in which the incident beam is scattered only weakly. In this limit, the

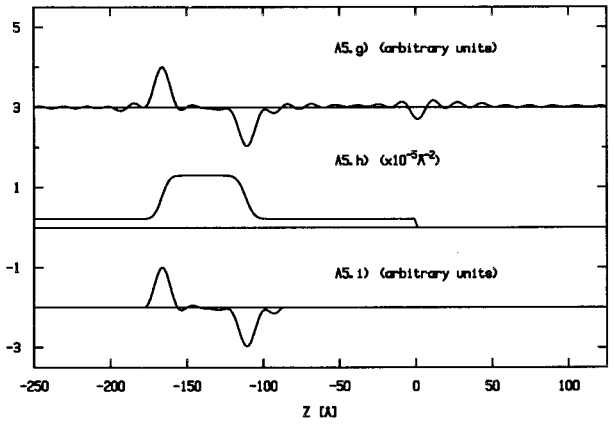

FIGURE 12 (*A5g*) Neutron scattering length density gradient obtained from highly constrained box refinement. A neutron scattering length density was constructed using model refinement (*A5h*). The scattering length density gradient was set to zero outside of its internal structure and used as a trial reference profile for refinement of the composite substrate plus SAM plus protein structure.

scattering potential and the scattering amplitude are Fourier-inverse Fourier transform pairs (the first Born approximation). This approximation is valid except for very small values of momentum transfer as q_z approaches q_{critical} where multiple scattering effects have been neglected in the kinematical approach (for a thorough discussion, see the Appendix of Lösche et al., 1993). Equations A1a and A1b below show that in the usual reflectivity formalism, in the first Born approximation, this is true of the gradient of the neutron scattering length density profile and the normalized reflectivity (Als-Nielsen et al., 1982; Braslau et al., 1988; Tidswell et al., 1990; Als-Nielsen et al., 1994):

$$R(q_z) = R_F(q_z)|\Phi(q_z)|^2, \tag{A1a}$$

where

$$\Phi(q_z) = \int (1/\rho_\infty)[d\langle\rho\rangle/dz]\exp(2\pi i q_z z)dz. \tag{A1b}$$

Because the gradient of the neutron scattering length density profile structure $[d\langle\rho\rangle/dz]$ is also finite in extent, we can apply the constrained box-refinement algorithm to the normalized reflectivity data $|\Phi(q_z)|^2$ to recover this function employing the well-known Fresnel reflectivity $R_F(q_z)$ for a uniform substrate with an infinitely sharp interface at its surface.

Third, the solution space is further constrained by utilizing a reference profile structure. The reference structure is developed by fabricating a multilayer substrate (to which the unknown sample structure will be attached) that has distinct features in its profile structure produced by alternating layers of materials possessing substantially different scattering contrast. Its profile structure is known at least approximately from its fabrication specifications. Because we are working with normalized reflectivity here, the gradient of the reference profile structure is calculated and refined against its normalized reflectivity data. The surface features of the substrate are truncated from the gradient profile, leaving the internal features of the gradient profile as the trial structure for initiating the box-refinement algorithm applied to the normalized reflectivity data from the composite structure. There should be little or no change in these internal features upon attaching the unknown sample structure onto the substrate surface to form the composite structure.

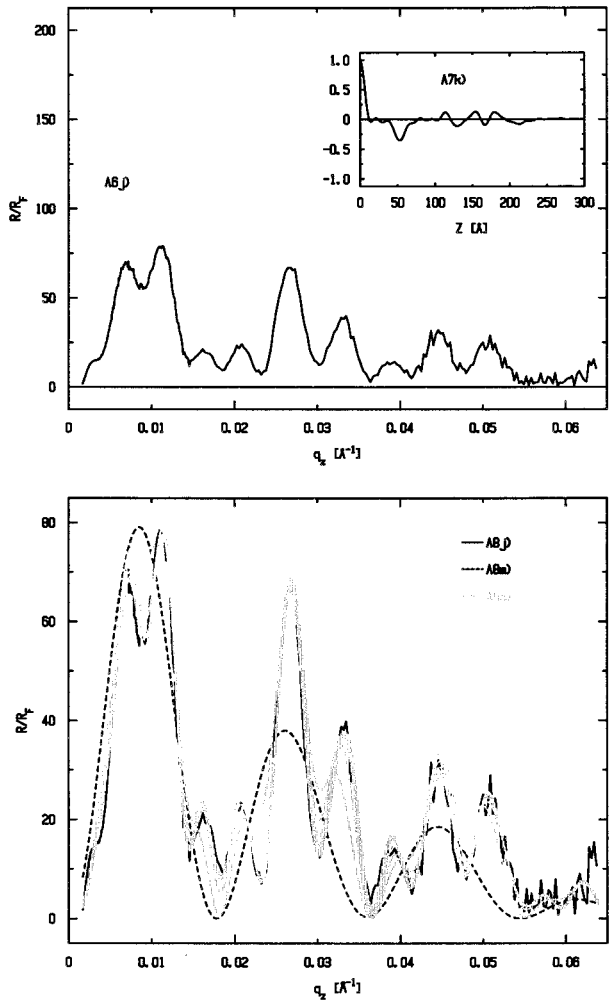

FIGURE 13 Normalized reflectivity for the composite substrate plus SAM plus protein/D_2O system (*A6j*) and the Patterson function calculated from this reflectivity (*inset*, *A7k*). (*A8*) Comparison of the experimental (*A8j*) and calculated normalized reflectivities (*A8m* and *A8n*). The reflectivity of the trial structure is shown as a dashed line, and the calculated reflectivities for each iteration of the refinement are shown in gray. Note that the refinement converges after five iterations.

Thus, the highly constrained box-refinement algorithm provides a method for transforming the initial reference profile structure into a profile structure that predicts the experimentally observed reflectivity for the composite structure exactly. The heart of the box-refinement algorithm is the box constraint: the correct solution will be finite in extent and of the same size as the actual structure. This size can be obtained from the experimental normalized reflectivity data without any assumptions by computing its inverse Fourier transform. This operation yields the autocorrelation function of the derivative of the neutron scattering length density profile (or the Patterson function). If the gradient of the profile structure has a thickness L, the significant oscillations in the Patterson function in excess of the $(q_z)_{\max}$ truncation ripple will die out beyond $+|L|$, as correlations cannot extend over distances larger than the gradient of the profile structure itself.

The estimated thickness of the gradient of the profile structure, the box constraint, is a key input to the algorithm. We also input the square root of the experimental normalized reflectivity function, $|\Phi_{\text{exp}}(q_z)|$, which is the magnitude of the Fourier transform of the gradient of the neutron scattering

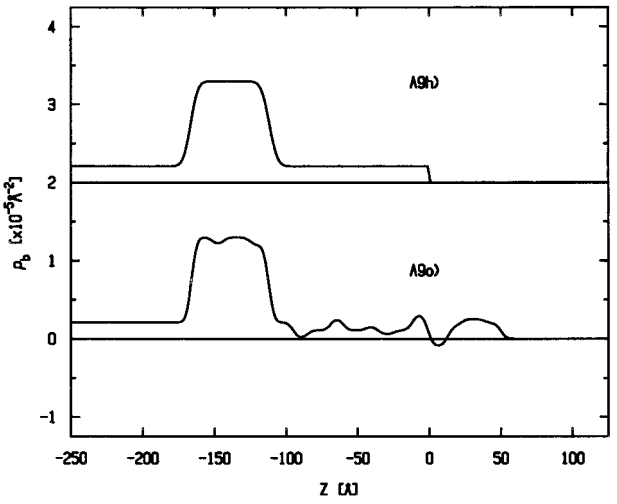

FIGURE 14 The final neutron scattering length density models for the bare substrate (*A9h*) and the composite system (*A9o*).

length density profile $d\rho/dz$ of the composite profile structure. We start the algorithm with the trial structure, $(d\rho/dz)_0$, the gradient of the reference profile structure, and compute its Fourier transform. We discard the magnitude of the Fourier transform but retain the resulting phase function, ϕ_1, neglecting its argument q_z. We use ϕ_1 to compute the inverse Fourier transform of $|\Phi_{exp}(q_z)|$ and thereby obtain a new structure, $(d\rho/dz)_1$. At this point, we apply the box constraint. The portion of $(d\rho/dz)_1$ that lies outside of $0 < z < L$ is set to zero to get the truncated $(d\rho/dz)_{1t}$. Now we compute the Fourier transform of $(d\rho/dz)_{1t}$. We check the progress of the refinement by comparing the modulus square of this Fourier transform with $|\Phi_{exp}(q_z)|^2$. If the agreement is poor (as is generally the case after the first iteration), we repeat the procedure with $(d\rho/dz)_{1t}$ as the input trial structure. We take the phase from its Fourier transform and compute the inverse Fourier transform of $|\Phi_{exp}(q_z)|$ to obtain $(d\rho/dz)_2$; we apply the box constraint to get $(d\rho/dz)_{2t}$; we compute the Fourier transform and compare its modulus square to $|\Phi_{exp}(q_z)|^2$ to check the progress of the refinement; if necessary, $(d\rho/dz)_{2t}$ becomes the input trial structure for the next iteration, and so on. The algorithm converges when the agreement between $\Phi_{exp}(q_z)^2$ and the modulus square of the Fourier transform of $(d\rho/dz)_n$ is good and there is little change between $(d\rho/dz)_n$ and $(d\rho/dz)_{n+1}$.

To demonstrate the method here, we will use the analysis steps that yielded the nonpolar SAM YCC/D_2O profile structure presented in this paper. (Note that the various experimental and calculated functions have been assigned lowercase letters, which appear on the relevant figure parts.) We begin with the normalized reflectivity for the bare substrate (Fig. 10 *A1a*). We then calculate its Patterson function (Fig. 10 *A2b*) to obtain the size of the box constraint. Next we calculate a model profile structure for the reference multilayer substrate based on its fabrication specifications using a procedure called model refinement. This consists of optimizing the model's parameters to produce an absolute neutron scattering length density model profile (Fig. 11 *A3c*) whose gradient (Fig. 11 *A3d*) has a Fourier transform modulus squared (Fig. 11 *A4e*) that is similar to the experimental normalized reflectivity data (Fig. 11 *A4a*). This gradient profile is then used as a trial structure for constrained box refinement. Box refinement yields a calculated normalized reflectivity $|\Phi_{calc}(q_z)|^2$ and a neutron scattering length density gradient for each iteration. Convergence is determined by comparing the calculated $|\Phi_{calc}(q_z)|^2$ for a given iteration (e.g., Fig. 11 *A4f*) with the experimental normalized reflectivity (Fig. 11 *A4a*). The converged neutron scattering length density gradient (Fig. 12 *A5g*) is then truncated (set to zero) outside its internal structure (which should be unchanged by the deposition of the SAM and protein monolayer on its surface), and the resulting function (Fig. 12 *A5i*) is used as a trial reference profile structure for constrained refinement of the data for the composite substrate plus SAM plus protein structure.

Once again the normalized reflectivity for the composite substrate plus SAM plus protein structure (Fig. 13 *A6j*) is inverse Fourier transformed to yield the Patterson function (Fig. 13 *A7k*), which clearly extends farther than the Patterson for the bare substrate (Fig. 10 *A2b*). Now we input the box constraint for the composite structure, the trial reference profile structure gradient (Fig. 12 *A5i*), and the experimental $|\Phi_{exp}(q_z)|^2$ for the composite structure (Fig. 13 *A6j*) into the refinement algorithm. In Fig. 13 *A8* we see the convergence from a clearly incorrect normalized reflectivity $|\Phi_{calc}(q_z)|^2$ (Fig. 13 *A8m*, which was calculated directly from the trial structure) to a calculated normalized reflectivity $|\Phi_{calc}(q_z)|^2$ (Fig. 13 *A8n*), which exactly matches the experimental normalized reflectivity to within the counting statistics. Finally, an absolute neutron scattering density profile model (Fig. 14 *A9o*) is refined whose gradient profile, Fourier-inverse Fourier transformed employing the experimental q_z window, exactly matches the output neutron scattering length density gradient from constrained refinement, as shown in the upper right quadrant of Fig. 5. This is the profile structure for the composite Si/Fe/Si/nonpolar SAM/YCC, D_2O system reported in this paper.

REFERENCES

Als-Nielsen, J., F. Christensen, and P. S. Pershan. 1982. Smectic-A order at the surface of a nematic liquid crystal: synchrotron x-ray diffraction. *Phys. Rev. Lett.* 48:1107–1110.

Als-Nielsen, J., D. Jacquemain, K. Kjaer, F. Leveiller, M. Lahav, and L. Leiserowitz. 1994. Principles and applications of grazing incidence x-ray and neutron scattering from ordered molecular monolayers at the air-water interface. *Phys. Rep.* 246:251–313.

Braslau, A., P. S. Pershan, G. Swislow, B. M. Ocko, and J. Als-Nielsen. 1988. Capillary waves on the surface of simple liquids measured by x-ray reflectivity. *Phys. Rev. A.* 38:2457–2470.

Chupa, J. A., J. P. McCauley, R. M. Strongin, A. B. Smith, J. K. Blasie, L. J. Peticolas, and J. C. Bean. 1994. Vectorially-oriented membrane protein monolayers: profile structures determined via x-ray interferometry/holography. *Biophys. J.* 67:336–348.

Edwards, A. M., J. K. Blasie, and J. C. Bean. 1998. Vectorially -oriented monolayers of the cytochrome c/cytochrome oxidase bimolecular complex. *Biophys. J.* 74:1346–1357.

Lesslauer, W., and J. K. Blasie. 1971. X-ray holographic interferometry in the determination of planar multilayer structures: theory and experimental observations. *Acta Crystallogr.* A27:456–461.

Lösche, M., M. Piepenstock, A. Diedrich, T. Grünewald, K. Kjaer, and D. Vaknin. 1993. Influence of surface chemistry on the structural organization of macromolecular protein layers adsorbed to functionalized aqueous interfaces. *Biophys. J.* 65:2160–2177.

Majkrzak, C. F., and N. F. Berk. 1995. Exact determination of the phase in neutron reflectometry. *Phys. Rev. B.* 5210827–10830.

Makowski, L. 1981. The use of continuous diffraction data as a phase constraint. I. One-dimensional theory. *J. Appl. Cryst.* 14:160–168.

Milne, J. S., L. Mayne, H. Roder, A. J. Wand, and S. W. Englander. 1997. Determinants of protein hydrogen exchange studied in equine cytochrome c. *Protein Sci.* 7:739–745.

Murphy, M. A., J. K. Blasie, L. J. Peticolas, and J. C. Bean. 1993. X-ray interferometry/holography for the unambiguous determination of the profile structures of single Langmuir-Blodgett monolayers. *Langmuir.* 9:1134–1141.

Pachence, J. M., S. M. Amador, G. Maniara, J. Vanderkooi, P. L. Dutton, and J. K. Blasie. 1990. Orientation and lateral mobility of cytochrome c on the surface of ultrathin lipid multilayer films. *Biophys. J.* 58: 379–389.

Pachence, J. M., and J. K. Blasie. 1991. Structural investigation of the covalent and electrostatic binding of yeast cytochrome c to the surface of various ultrathin lipid multilayers using x-ray diffraction. *Biophys. J.* 59:894–900.

Prokop, L. A., R. M. Strongin, A. B. Smith III, J. K. Blasie, L. J. Peticolas, and J. C. Bean. 1996. Vectorially oriented monolayers of detergent-solubilized Ca^{2+}-ATPase from sarcoplasmic reticulum. *Biophys. J.* 70: 2131–2143.

Stroud, R. M., and D. A. Agard. 1979. Structure determination of asymmetric membrane profiles using an iterative Fourier method. *Biophys. J.* 25:495–512.

Tidswell, I. M., B. M. Ocko, P. S. Pershan, S. R. Wasserman, G. M. Whitesides, and J. D. Axe. 1990. X-ray specular reflection studies of silicon coated by organic monolayers (alkylsiloxanes). *Phys. Rev. B.* 41:1111–1128.

Xu, S., R. F. Fischetti, J. K. Blasie, L. J. Peticolas, and J. C. Bean. 1993. Profile and in-plane structures of self-assembled monolayers on Ge/Si multilayer substrates by high resolution x-ray diffraction employing x-ray interferometry/holography. *J. Phys. Chem.* 97:1961–1969.

Xu, S., M. A. Murphy, S. M. Amador, and J. K. Blasie. 1991. Proof of the asymmetry in the Cd-arachidate bilayers of ultrathin Langmuir-Blodgett multilayer films via x-ray interferometry. *J. Phys. I France.* 1:1131–1144.

Zaccai, G., J. K. Blasie, and B. P. Shoenborn. 1975. Neutron diffraction studies on the location of water in lecithin bilayer model membranes. *Proc. Natl. Acad. Sci. U.S.A.* 72:376–380.